

Article

Characteristics of Aerosol during a Severe Haze-Fog Episode in the Yangtze River Delta: Particle Size Distribution, Chemical Composition, and Optical Properties

Ankang Liu ¹, Honglei Wang ^{1,2,3,*}, Yi Cui ¹, Lijuan Shen ¹, Yan Yin ¹, Zhijun Wu ², Song Guo ², Shuangshuang Shi ¹, Kui Chen ¹, Bin Zhu ¹, Jinhu Wang ¹  and Xiangchen Kong ⁴

- ¹ Collaborative Innovation Center on Forecast and Evaluation of Meteorological Disasters, Key Laboratory for Aerosol-Cloud-Precipitation of China Meteorological Administration, Nanjing University of Information Science & Technology, Nanjing 210044, China; 20181203017@nuist.edu.cn (A.L.); 20171202164@nuist.edu.cn (Y.C.); 20181103046@nuist.edu.cn (L.S.); yinyan@nuist.edu.cn (Y.Y.); sss@nuist.edu.cn (S.S.); 001489@nuist.edu.cn (K.C.); binzhu@nuist.edu.cn (B.Z.); goldtigerwang@nuist.edu.cn (J.W.)
- ² State Key Joint Laboratory of Environment Simulation and Pollution Control (Peking University), College of Environmental Sciences and Engineering, Peking University, Beijing 100871, China; zhijunwu@pku.edu.cn (Z.W.); songguo@pku.edu.cn (S.G.)
- ³ State Key Laboratory of Atmospheric Boundary Layer Physics and Atmospheric Chemistry, Institute of Atmospheric Physics, Chinese Academy of Sciences, Beijing 100029, China
- ⁴ Ordos Meteorological Bureau of Inner Mongolia, Ordos 017000, China; 15147736650m@sina.cn
- * Correspondence: hongleiwang@nuist.edu.cn

Received: 1 December 2019; Accepted: 24 December 2019; Published: 2 January 2020



Abstract: Particle size distribution, water soluble ions, and black carbon (BC) concentration in a long-term haze-fog episode were measured using a wide-range particle spectrometer (WPS), a monitor for aerosols and gases (MARGA), and an aethalometer (AE33) in Nanjing from 16 to 27 November, 2018. The observation included five processes of clean, mist, mix, haze, and fog. Combined with meteorological elements, the HYSPLIT model, and the IMPROVE model, we analyzed the particle size distribution, chemical composition, and optical properties of aerosols in different processes. The particle number size distribution (PNSD) in five processes differed: It was bimodal in mist and fog and unimodal in clean, mix, and haze. The particle surface area size distribution (PSSD) in different processes showed a bimodal distribution, and the second peak of the mix and fog processes shifted to a larger particle size at 480 nm. The dominant air masses in five processes differed and primarily originated in the northeast direction in the clean process and the southeast direction in the haze process. In the mist, mix, and fog processes local air masses dominated. NO_3^- was the primary component of water soluble ions, with the lowest proportion of 45.6% in the clean process and the highest proportion of 53.0% in the mix process. The ratio of NH_4^+ in the different processes was stable at approximately 23%. The ratio of SO_4^{2-} in the clean process was 26.2%, and the ratio of other processes was approximately 20%. The average concentration of BC in the fog processes was $10,119 \text{ ng}\cdot\text{m}^{-3}$, which was 3.55, 1.80, 1.60, and 1.46 times that in the processes of clean, mist, mix, and haze, respectively. In the different processes, BC was primarily based on liquid fuel combustion. NO_3^- , SO_4^{2-} , and BC were the main contributors to the atmospheric extinction coefficient and contributed more than 90% in different processes. NO_3^- contributed 398.43 Mm^{-1} in the mix process, and SO_4^{2-} and BC contributed 167.90 Mm^{-1} and 101.19 Mm^{-1} , respectively, during the fog process.

Keywords: aerosol; size distribution; chemical composition; optical properties; Yangtze River Delta

1. Introduction

Anthropogenic aerosols include nitrates, sulfates, ammonium salts, black carbon, organic matter, and dust [1,2]. Aerosols affect the earth's radiation balance and climate by directly scattering and absorbing solar and terrestrial radiation, and indirectly modifying clouds and precipitation by acting as cloud condensation nuclei (CCN) [3–5]. In the boundary layer, aerosol particles can accumulate and cause air pollution in unfavorable dispersion conditions, and then produce adverse effects on human health and atmospheric visibility [6–8]. Haze is an atmospheric phenomenon in which the sky clarity is obscured by a large number of fine dry particles, during which the atmospheric visibility and relative humidity (RH) are usually less than 5 km and 80% [9,10]. When more water vapor exists in the air, some dry aerosol particles with strong water absorption will develop and eventually be activated into the CCN [11,12], which produces a larger quantity of fog droplets with a smaller size, which further reduce the visibility. Currently, the atmospheric visibility is usually less than 1 km and the RH is greater than 90% [13]. With frequent human activities, the haze problem in the central and eastern regions of China has become increasingly significant in the past two or three decades [14–18], which is attributed to the significant increase in atmospheric aerosols emitted by humans [19,20].

The Yangtze River Delta (YRD), with Shanghai as its center and 26 cities in Jiangsu, Zhejiang, and Anhui province, is one of the most economically developed and densely populated regions in China. Several haze-fog episodes with sulfate, nitrate, ammonium, and organic aerosol as major components have been observed in the YRD [21–24]. High pressure system, subsidence airflow, and calm surface wind are responsible for the decrease of the planetary boundary layer (PBL) and the accumulation of pollutants [25]. The high extinction coefficient in the YRD is attributed to the aerosol mass concentration and is affected by the aerosol chemical component, PNSD, and water vapor [26]. Higher accumulation mode particle counts, and higher RH were the main reasons for the decrease of atmospheric visibility [27–29]. The transformation of SO₂ and NO₂, which primarily originated from fossil fuel combustion and vehicle emissions, contributed a substantial amount to the high concentration of secondary nitrate and sulfate in the YRD [30–32].

During the transition from haze to fog, the concentrations of smaller particles (less than 0.060–0.090 μm) decreased, the concentrations of larger particles increased, and the temporal variation in the aerosol number concentration negatively correlated with the root mean square of diameters during the observation period [33]. The particle growth process was attributed to the nitrate and organics components, which were driven by the processes of secondary aerosol formation and air mass origin [34]. The wet deposition of aerosol particles by fog droplets is strong in the long-term maintenance of fog [35]. However, the short duration of fog is not sufficient for removing most aerosol particles from the atmosphere via wet deposition [36]. With the dissipation of fog, new aerosol particles are formed after the evaporation of fog droplets that undergo heterogeneous chemical reactions. These newly generated aerosol particles usually have strong moisture absorption and form haze at a higher concentration [37].

Previous studies of haze in the YRD have divided the haze-fog process. However, the study of pollutant characteristics remains divided into clean, haze, and fog days for comparison, which disregard the mutual transformation of fog and haze in daily variation. Relatively few studies have explored the distribution characteristics of chemical components in the transition of haze and fog. In this study, we use high-resolution online monitoring instruments to further refine the haze, fog, and transformation processes and explore the characteristics of pollutant components at different stages. A comprehensive observation of submicron aerosols was conducted in Nanjing from 16 November, 2018 to 27 November, 2018. Combined with the meteorological elements, reactive gases, and aerosol chemical composition and optical model, the particle size distribution, chemical composition, and optical properties of aerosols in different processes were analyzed.

2. Experimental Methods

2.1. Description of the Observation Site

Figure 1 shows that the observation site is located on top of the meteorological building, which is approximately 40 m above the ground and 62 m above sea level, at Nanjing University of Information Science and Technology (NUIST, 32.207° N, 118.717° E). A highway is approximately 500 m east of the sampling site, and the daily traffic volumes exceed 50,000 [38]. NUIST is adjacent to the Gaoxin Development Zone and located at the foot of Long Wang Mountain. The area from 3 km to 10 km in the southeast region gathers heavy pollution enterprises such as chemical, steel, and electric power. Therefore, this sampling site represents the air pollution situation in the mixed industrial area in the northern suburb of Nanjing.

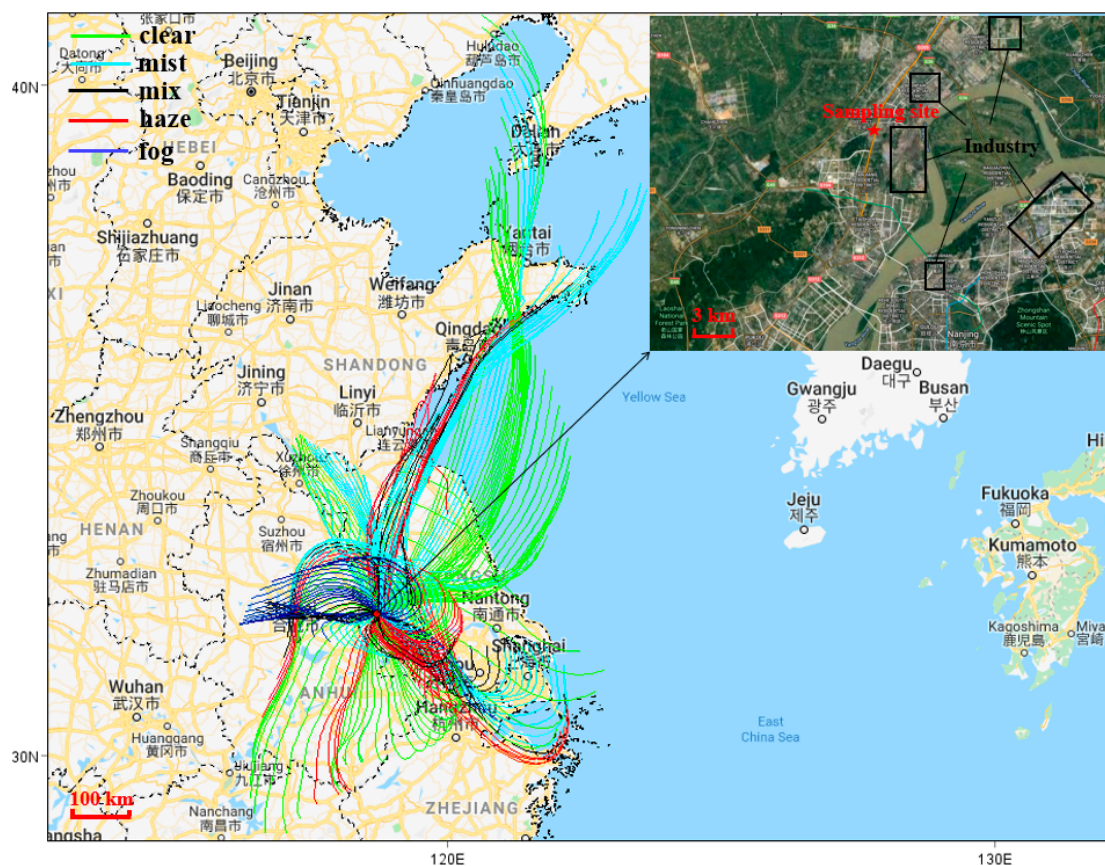


Figure 1. Observation site and 24 h backward trajectory at 500 m altitude.

2.2. Description of Observational Instruments

The water soluble ions observation instrument used was the monitor for aerosols and gases (MARGA ADI 2080) manufactured by the Metrohm Corporation of Switzerland. Fine particulate matter $PM_{2.5}$ was sampled. The MARGA is divided into three parts: Sampling, analysis, and integrated control. This instrument can continuously observe the concentrations of water soluble ions (Cl^- , NO_3^- , SO_4^{2-} , NH_4^+ , Na^+ , K^+ , Mg^{2+} , and Ca^{2+}) and trace gases (HCl, HNO_2 , HNO_3 , SO_2 , and NH_3) in aerosols. The detection limits of each component is 0.01, 0.05, 0.04, 0.05, 0.05, 0.09, 0.06, 0.09, 0.01, 0.02, 0.05, 0.03, and $0.05 \mu g \cdot m^{-3}$, respectively, and the time resolution is 1 h. A detailed description of the principles of the instrument are detailed in the literature [39].

The aerosol number concentrations from 5 nm to 10 μm were measured using a wide-range particle spectrometer (WPS) manufactured by MSP Corporation (Shoreview, MN, USA), with a time resolution of 5 min. The instrument consists of differential mobility analysis (DMA), condensation

particle counting (CPC), and laser light scattering (LPS). The measurement range of the first two processes is 5 nm–0.5 μm , and that of the LPS is 0.35–10 μm . Due to the different measuring principles, the observed values within the cross-measuring range (0.35–0.5 μm) differ. The specific principles of the instrument are provided in the literature [40].

The black carbon concentration was measured using the aethalometer (AE33) produced by Magee Corporation (Matthews, NC, USA). The AE33 provides a real-time optical measurement of light absorbing carbonaceous aerosols at seven channels ($\lambda = 940, 880, 660, 590, 525, 470,$ and 370 nm). Due to the least interference from other substances at 880 nm, the measurement results of the 880 nm channel were adopted as the concentration of BC. The sampling particle size of the instrument is 2.5 μm , the sampling flow is 5 $\text{L}\cdot\text{min}^{-1}$, and the data were obtained every 5 min.

The data of $\text{PM}_{2.5}$ was observed by a β -ray dust meter (Model 5030 SHARP) manufactured by the Thermo Fisher Scientific (Waltham, MA, USA), and the principle of the instrument is described in the reference [41]. The pollution gas data were obtained from the average pollutant concentration data of Nanjing City in the real-time release platform of China's urban air quality (<http://106.37.208.233:20035>). The meteorological data were obtained from the comprehensive meteorological observation base in NUIST, where the linear distance from the sampling site is 1.1 km. The meteorological data include the relative humidity, temperature, wind direction, wind speed, visibility, and precipitation. The time resolution is 1 h. The backward trajectory was drawn by MeteInfo 1.9.0 (<http://www.meteothink.org/products/index.html>), using the Hybrid Single Particle Lagrangian Integrated Trajectory Model (HYSPLIT model).

2.3. Data Validity Analysis

The sampling process was conducted from 16 November, 2018 to 27 November, 2018. A total of 288 groups of samples were obtained by hour, and 255 groups of effective samples were retained after excluding data that contained precipitation. According to the anion equivalent concentration Equation (Equation (1)) and the cation equivalent concentration Equation (Equation (2)) [42], the correlation between anions and cations in water soluble ions was calculated. Figure 2 shows that the correlation between anions and cations is high, $y = 1.092x - 0.023$, and $R^2 = 0.992$, which indicates that the analyzed ions adequately represent the main water soluble ions in $\text{PM}_{2.5}$. The slope of the linear dispersion between anions and cations is greater than 1, which indicates that the water soluble ions are weakly alkaline, and the cation equivalent concentration in the sample is slightly higher than that of the anion, which is consistent with previous observations in Nanjing [43].

$$\text{AE} = \frac{\text{Cl}^-}{35.5} + \frac{\text{NO}_3^-}{62} + \frac{\text{SO}_4^{2-}}{48}. \quad (1)$$

$$\text{CE} = \frac{\text{NH}_4^+}{18} + \frac{\text{Na}^+}{23} + \frac{\text{K}^+}{39} + \frac{\text{Mg}^{2+}}{12} + \frac{\text{Ca}^{2+}}{20}. \quad (2)$$

2.4. Aerosol Acidity

To evaluate the acidity of $\text{PM}_{2.5}$, the molar concentration of hydrogen ion (H^+) was calculated using Equation (3). The acidity of aerosol f is usually evaluated by the ratio of the concentration of H^+ to the sum of all cation concentrations (Equation (4)). $f \leq 0$ means that each mole of SO_4^{2-} , NO_3^- , and Cl^- is completely neutralized by cations. $f = 1$ means that no neutralization reaction occurs, and SO_4^{2-} , NO_3^- , and Cl^- is likely to exist in the form of H_2SO_4 , HNO_3 , and HCl , respectively [44].

$$[\text{H}^+] = 2[\text{SO}_4^{2-}] + [\text{NO}_3^-] + [\text{Cl}^-] - [\text{NH}_4^+] - [\text{Na}^+] - [\text{K}^+] - 2[\text{Mg}^{2+}] - 2[\text{Ca}^{2+}]. \quad (3)$$

$$f = \frac{[\text{H}^+]}{[\text{H}^+] + [\text{NH}_4^+] + [\text{Na}^+] + [\text{K}^+] + 2[\text{Mg}^{2+}] + 2[\text{Ca}^{2+}]}. \quad (4)$$

In the Equation, [] means the molar concentration of its corresponding component ($\mu\text{mol}\cdot\text{m}^{-3}$).

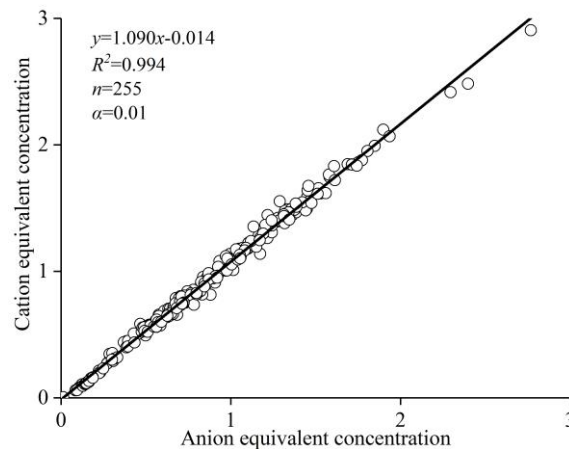


Figure 2. The correlation between anion equivalent concentration and cation equivalent concentration.

2.5. Nitrogen Oxidation Ratio (NOR) and Sulfur Oxidation Ratio (SOR)

NOR and SOR are usually employed to reflect the degree of secondary transformation of NO_2 and SO_2 . The larger the values of NOR and SOR, the more NO_2 and SO_2 transform to secondary aerosol particles by gas-liquid phase oxidation in the atmosphere. The Equation for NOR and SOR is expressed as follows [45]:

$$\text{NOR} = \frac{[\text{NO}_3^-]}{[\text{NO}_3^-] + [\text{NO}_2]} \quad (5)$$

$$\text{SOR} = \frac{[\text{SO}_4^{2-}]}{[\text{SO}_4^{2-}] + [\text{SO}_2]} \quad (6)$$

In the Equation, [] means the molar concentration of its corresponding component ($\mu\text{mol}\cdot\text{m}^{-3}$).

2.6. Absorption Coefficients for Liquid and Solid Fuel-Sourced BC

The total light absorption coefficients at 880 nm is generally considered to be caused by the BC produced by the combustion of liquid fuels and solid fuels (coal and biomass burning). According to previous studies [46,47], the portion (p) of the BC contribution from the liquid fuel sources and the light absorption exponent (α) can be calculated by using the BC mass concentration measured at the 370 nm and 880 nm channels of AE33:

$$p = \frac{\text{BC6} - \left(\frac{370}{880}\right)^2 \times \frac{18.47 \times \text{BC1}}{7.77}}{\text{BC6} \times \frac{510}{880}} \quad (7)$$

$$\alpha = \log_{10} \frac{\text{BC6} \times 7.77}{\text{BC1} \times 18.47} / \log_{10} \frac{370}{880} \quad (8)$$

In the Equation, BC6 is the concentration measured by the AE33 instrument at 880 nm, and BC1 is the concentration measured at 370 nm.

2.7. IMPROVE Model

To study the contribution of the observed $\text{PM}_{2.5}$ components to aerosol extinction, the modified IMPROVE model [48] was used to calculate the effect of the observed components on the atmospheric extinction coefficient:

$$\beta_{\text{ext}} = 3f(RH)[\text{AN} + \text{AS}] + 4[\text{OM}] + 10[\text{EC}] + 1[\text{Soil}] + 1.77f(RH)[\text{SS}] + 10. \quad (9)$$

where, $[]$ is the mass concentration of each component ($\mu\text{g}\cdot\text{m}^{-3}$) and $f(RH)$ is the growth factor of relative humidity, which changes with the change in the relative humidity [49]. $[AS] = 1.375 \times [SO_4^{2-}]$, $[AN] = 1.29 \times [NO_3^-]$, $[OM] = 1.4 \times [OC]$, $[Soil] = 1.63 \times [Ca^{2+}] + 1.67 \times [Mg^{2+}]$, and $[SS] = 1.8 \times [Cl^-]$.

In previous studies [34,50,51], the actual atmospheric extinction coefficient was usually calculated by the Koschmieder relation [52] and visibility data. The modified Koschmieder relation [53] was employed in this study:

$$\beta_{ext-vis} = 1.9/\text{visibility}. \tag{10}$$

3. Results and Discussion

3.1. Overview of the Observations

Figure 3 shows that the RH exhibits a significant daily variation. It was low in daytime and high in nighttime during the observation, with an average value of $78.7 \pm 15.4\%$, which was conducive to the mutual transformation of different processes in a haze-fog episode. The wind direction was primarily north and east, and the maximum wind speed was $4.2 \text{ m}\cdot\text{s}^{-1}$ and the average wind speed was $1.2 \pm 0.8 \text{ m}\cdot\text{s}^{-1}$. The lower wind speed is related to the static and stable weather caused by the high pressure control on the ground during the observation, which is not conducive to the diffusion of pollutants [25]. The average visibility during the observation was $4.8 \pm 4.5 \text{ km}$, and the maximum visibility exceeded 10 km for only three days (November 16, 17, and 23). In the first three days of observation, the clean process was primarily affected by precipitation and mist appeared at night. Affected by solar radiation, the concentration of O_3 presents distinct diurnal variation characteristics, while other pollution gases were relatively stable. PNSD was distinctly affected by the wet removal of precipitation. Visibility initially increased and then decreased to attain a maximum of 24.9 km at 13:00 on 17 November, 2018. The average concentration of $PM_{2.5}$ was $24.2 \mu\text{g}\cdot\text{m}^{-3}$ on the first three days.

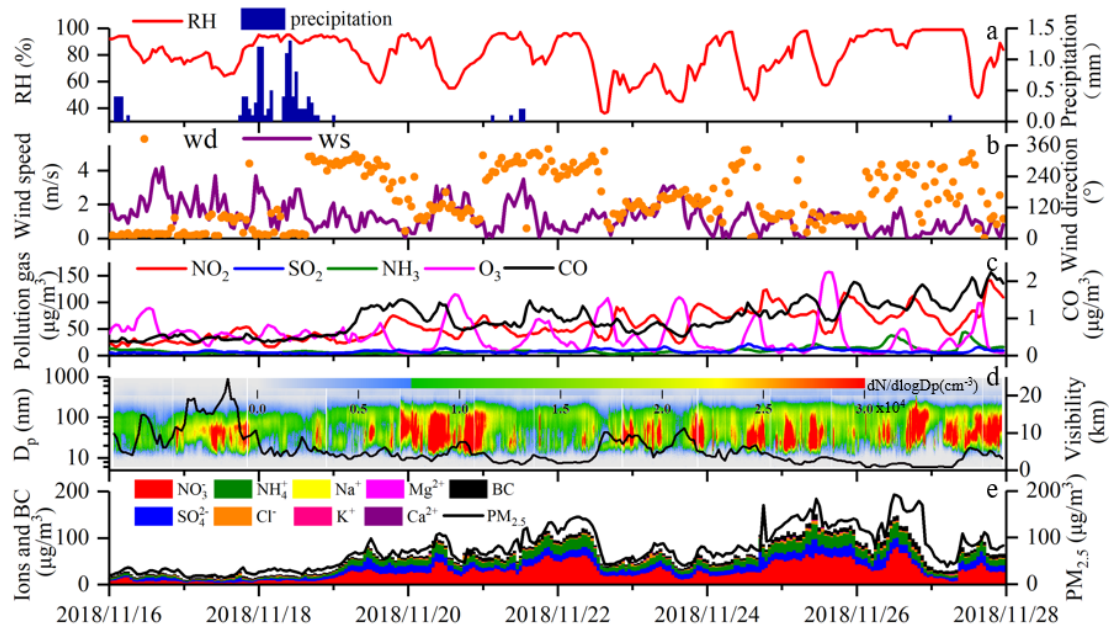


Figure 3. Time series of meteorological elements and pollutants.

The first pollution phase of the observation extended from 19 to 22 November, 2018. At 9:00 a.m. on 19 November, 2018, the first haze process occurred. The PNSD showed a distinctly high value area, which was concentrated within PM_1 , and the dominant particle size range ranged from 25 to 55 nm. As the mist dissipated at noon on 22 November, 2018, the RH rapidly decreased to 39% and the pollution decreased. The concentration of $PM_{2.5}$ decreased by more than $20 \mu\text{g}\cdot\text{m}^{-3}$ per hour and the weather was fine until the 23 November, 2018. From the 24 November 2018, the haze-fog pollution

reappeared and began to increase. The concentration of pollution gases fluctuated and increased, with the peak of $PM_{2.5}$ occurring at $191.5 \mu\text{g}\cdot\text{m}^{-3}$. A large area of fog persisted for 15 h in the YRD beginning the evening of the 26 November, 2018. The decrease in $PM_{2.5}$ mass concentration preceded the dissipation of fog, which indicates that the fog had a wet cleaning effect on particulate matter [54].

3.2. Classification in the Haze-Fog Episode

Figure 4a shows that $PM_{2.5}$ played a key role in low visibility ($<5 \text{ km}$) when RH was low ($<80\%$); the average value was $100.18 \mu\text{g}\cdot\text{m}^{-3}$. With high RH ($>90\%$), the concentration of $PM_{2.5}$ and visibility were both low, which was related to the hygroscopic growth of aerosol particles [55]. According to the Kohler equation, particles with radii of $1\text{--}10 \mu\text{m}$ can activate and grow beyond $10 \mu\text{m}$ or even form cloud droplets when the RH is less than 100% [56]. Combined with previous research and the characteristics of the target area and according to hourly data of visibility, RH and $PM_{2.5}$, the observation period was divided into five processes: Clean, mist, haze, mix, and fog. The specific classification criteria are listed as follows (Figure 4b): (1) clear: Visibility $> 5 \text{ km}$; (2) mist: $1 \text{ km} < \text{visibility} < 5 \text{ km}$ and $\text{RH} > 90\%$; (3) haze: Visibility $< 5 \text{ km}$ and $\text{RH} < 80\%$; (4) mix: Visibility $< 5 \text{ km}$ and $80\% < \text{RH} < 90\%$; and (5) fog: Visibility $< 1 \text{ km}$ and $\text{RH} > 90\%$.

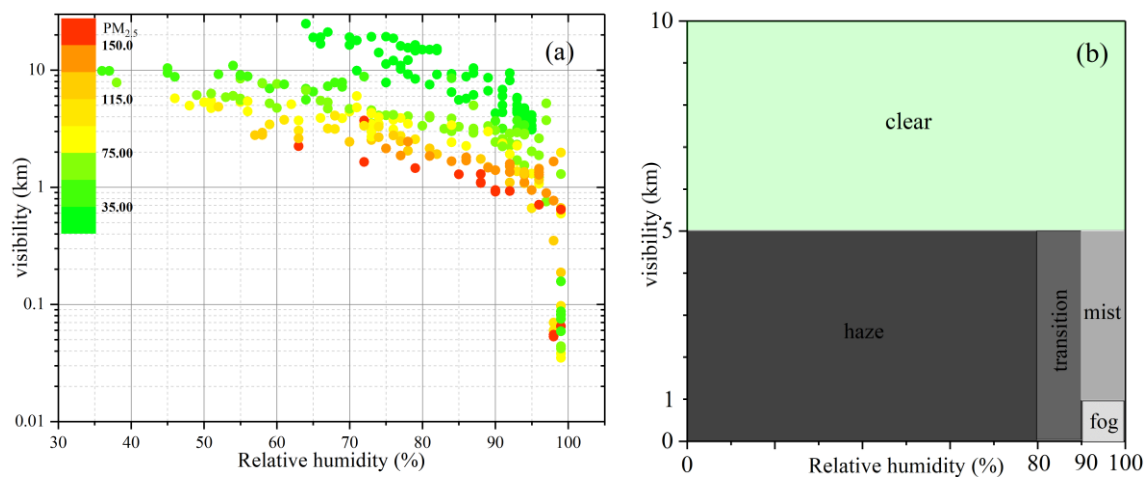


Figure 4. (a) the relation of visibility, Relative and $PM_{2.5}$ and (b) the classification in the haze-fog episode.

As shown in Table 1, the clean process occurred most frequently during this observation period and the frequency of fog occurrence was the lowest. Since the daily variation range of RH is usually large, the converting process from haze to fog or fog to haze may occur many times per day (including the process from haze to mist and mist to haze), which is classified as a mix process in this paper. The highest time of conversion was observed on the 19 and 25 November, 2018 and was seven times. The mean $PM_{2.5}$ concentration in the mix process was higher than that in other processes, and the mean value was $110.88 \mu\text{g}\cdot\text{m}^{-3}$.

Table 1. The occurrence frequency of different processes in the haze-fog episode and the corresponding mean $PM_{2.5}$ mass concentration.

Type	Visibility (km)	Relative Humidity (%)	$PM_{2.5}$ ($\mu\text{g}/\text{m}^3$)	Frequency (%)	Hours (h)
Clear	>5	—	42.47	31.76	81
Mist	$1\text{--}5$	>90	81.51	21.96	56
Haze	<5	<80	101.11	22.75	58
Mix	<5	$80\text{--}90$	110.88	12.94	33
Fog	<1	>90	107.21	10.59	27

3.3. Characteristics of Aerosol Particle Size Distribution in Different Processes

Figure 5 shows that the PNSD was unimodal in the clean, haze, and mix processes, and bimodal in the mist and fog processes. The mist process achieved the smallest peak values of $19,101 \text{ cm}^{-3}$ and $17,506 \text{ cm}^{-3}$, and the peak particle diameters were 30 nm and 87 nm, respectively. The peaks of the fog process were $25,660 \text{ cm}^{-3}$ and $23,186 \text{ cm}^{-3}$, and the particle diameters at peak were 36 nm and 87 nm, respectively. The peak value of the clean and mix processes was similar to that of the fog process, which was 1.32 times and 1.33 times, respectively, that of the mist process, and the peak particle diameters were 32 nm and 27 nm, respectively. The maximum peak value of the haze process was 1.59 times the mist process, and the diameter at peak was 32 nm. The main mode of the aerosol number concentration in different processes was Aitken mode (10–100 nm). The proportion of the particle number concentration in Aitken mode was 85.1%, 75.8%, 79.1%, 77.5%, and 73.5% in the processes of clean, mist, haze, mix, and fog, respectively. The dominant particle size of the clean process, mist process, haze process, mix process, and the fog process was 20–40 nm, 20–50 nm, 25–40 nm, 20–40 nm, and 25–55 nm, respectively.

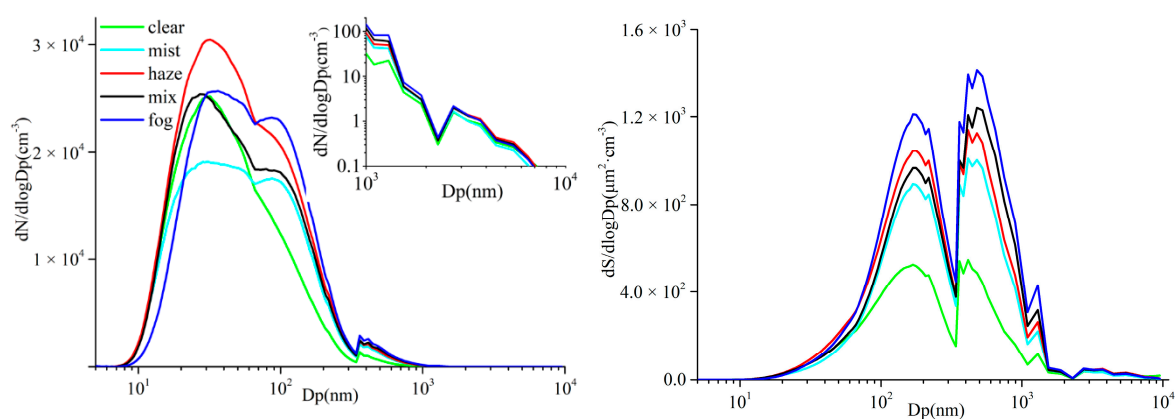


Figure 5. Particle number size distribution (PNSD) and particle surface area size distribution (PSSD) in different processes.

The PSSD showed a bimodal distribution in different processes. The particle size at the first peak was 169 nm and the peak value in the clean process was $524.32 \mu\text{m}^2 \cdot \text{cm}^{-3}$. The peak value in the processes of mist, haze, mix, and fog was 1.70 times, 1.99 times, 1.80 times, and 2.31 times that of the clean process, respectively. The particle size at the second peak was 415 nm in the processes of clean, mist, and haze, and 480 nm in the processes of mix and fog. The peak value in the clean process was $546.41 \mu\text{m}^2 \cdot \text{cm}^{-3}$, and the peak value of other processes was 1.84, 2.09, 2.27, and 2.59 times that of the clean process. The PSSD was related to the particle number concentration and RH. The second peak of the particle surface area concentration in the mix process exceeded that of the haze process, which indicates that the larger the particle size, the greater the surface area concentration of the aerosol affected by the RH.

3.4. Characteristics of Aerosol Chemical Composition in Different Processes

3.4.1. Distribution Characteristics of Water Soluble Ions in Different Processes

Figure 6 shows that the average mass concentration of water soluble ions in the clean process was $33.63 \mu\text{g} \cdot \text{m}^{-3}$, and the air mass in this process primarily originated in the northeast direction (Figure 2). The highest concentration of water soluble ions was observed in the mix process and was approximately 2.49 times that in the clean process. The air mass in the haze process primarily originated in the southeast, and the concentration of water soluble ions was 2.45 times that in the clean process, while the concentration of water soluble ions in the mist and fog process was only

1.78 times and 1.87 times that in the clean process, which may be related to the wet removal and local air mass control.

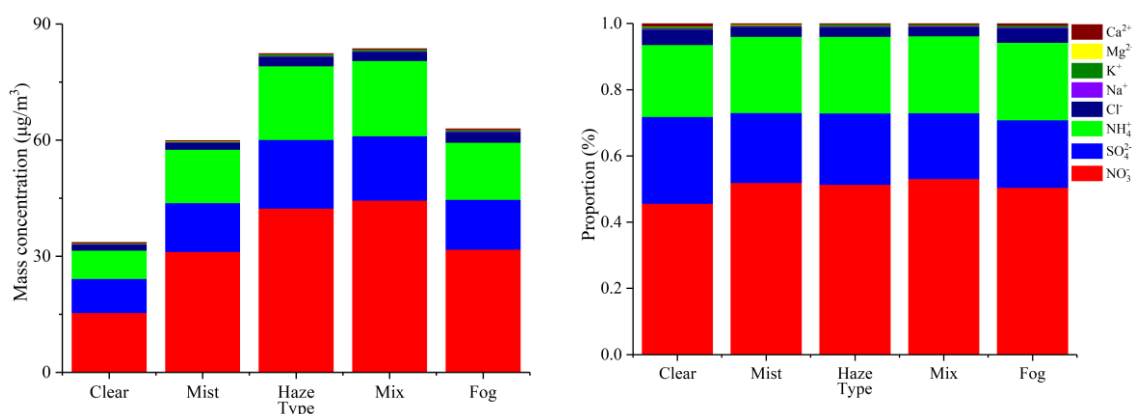


Figure 6. Mean mass concentration and proportion of water soluble ions in different processes.

NO_3^- was the primary component of water soluble ions in Nanjing, with the smallest proportion of 45.6% in the clean process and the largest proportion of 53.0% in the mix process. The highest average mass concentration of NO_3^- of $44.38 \mu\text{g}\cdot\text{m}^{-3}$ was observed in the mix process and was 2.89 times that in the clean process. The highest average mass concentration of SO_4^{2-} of $17.76 \mu\text{g}\cdot\text{m}^{-3}$ was observed in the haze process, and was 2.01 times that in the clean process. The SO_4^{2-} accounted for the most in the clean process with 26.2%, and the least in the mix process with 19.9%. The highest average mass concentration of NH_4^+ of $19.42 \mu\text{g}\cdot\text{m}^{-3}$ was observed in the mix process, which was 2.66 times that in the clean process. The variation in the proportion of NH_4^+ , which was approximately 23%, was stable in different processes.

The highest concentrations of Cl^- and Na^+ in the fog process were $2.70 \mu\text{g}\cdot\text{m}^{-3}$ and $0.19 \mu\text{g}\cdot\text{m}^{-3}$, which were approximately 1.77 times and 2.08 times that in the clean process. K^+ is generally considered as a tracer of biomass combustion, which has the highest concentration in the haze process. Mg^{2+} and Ca^{2+} exist in coarse particles, such as soil dust, with the largest proportion in the clean process.

Figure 7a shows that the aerosol acidity in the clean process was significantly higher than that in other processes during the observation. The H^+ concentration ranged from -0.06 to $0.15 \mu\text{mol}\cdot\text{m}^{-3}$, with an average value of $0.04 \mu\text{mol}\cdot\text{m}^{-3}$. The aerosol acidity f ranged from -0.11 to 0.51 , with an average value of 0.15 . The efficiency of the neutralization reaction was high in low visibility, which may be related to greater NH_4^+ dissolution with higher RH.

In relevant studies, the value of $\text{NO}_3^-/\text{SO}_4^{2-}$ is usually applied to indicate whether the nitrogen and sulfur in the atmosphere primarily originated from fixed sources or mobile sources. If the value of $\text{NO}_3^-/\text{SO}_4^{2-}$ is <1 , the fixed source is dominant; if the value of $\text{NO}_3^-/\text{SO}_4^{2-}$ is >1 , the mobile source is dominant [15]. Figure 7b shows that the average value of $\text{NO}_3^-/\text{SO}_4^{2-}$ in clean, mist, haze, mix, and fog during the observation period exceeded 1, which indicates that the main sources of nitrogen and sulfur in the haze-fog episode were mobile sources, and the clean process was slightly less affected by mobile sources than other processes, while the fog process was most affected by mobile sources.

The average values of NOR and SOR in different conditions during the observation period exceeded 0.1 (Figure 7c,d), which indicates that the nitrate and sulfate in $\text{PM}_{2.5}$ are mainly formed by secondary transformation during the observation period [57]. The relationship between the SOR and the RH was distinct and presented distinct stratification for different levels of RH. The SOR in the mist and fog with the highest RH was approximately 0.9. When the RH was low, the SOR was approximately 0.62 in the clean and haze processes. The smallest NOR of 0.25 was obtained in the clean process. The highest NOR, which was 1.55 times that in the clean process, was obtained in the mix process. The small NOR in mist and fog may be related to the large SOR in the case of the high RH, and the conversion of sulfate is higher, which makes NH_4^+ more bound to SO_4^{2-} .

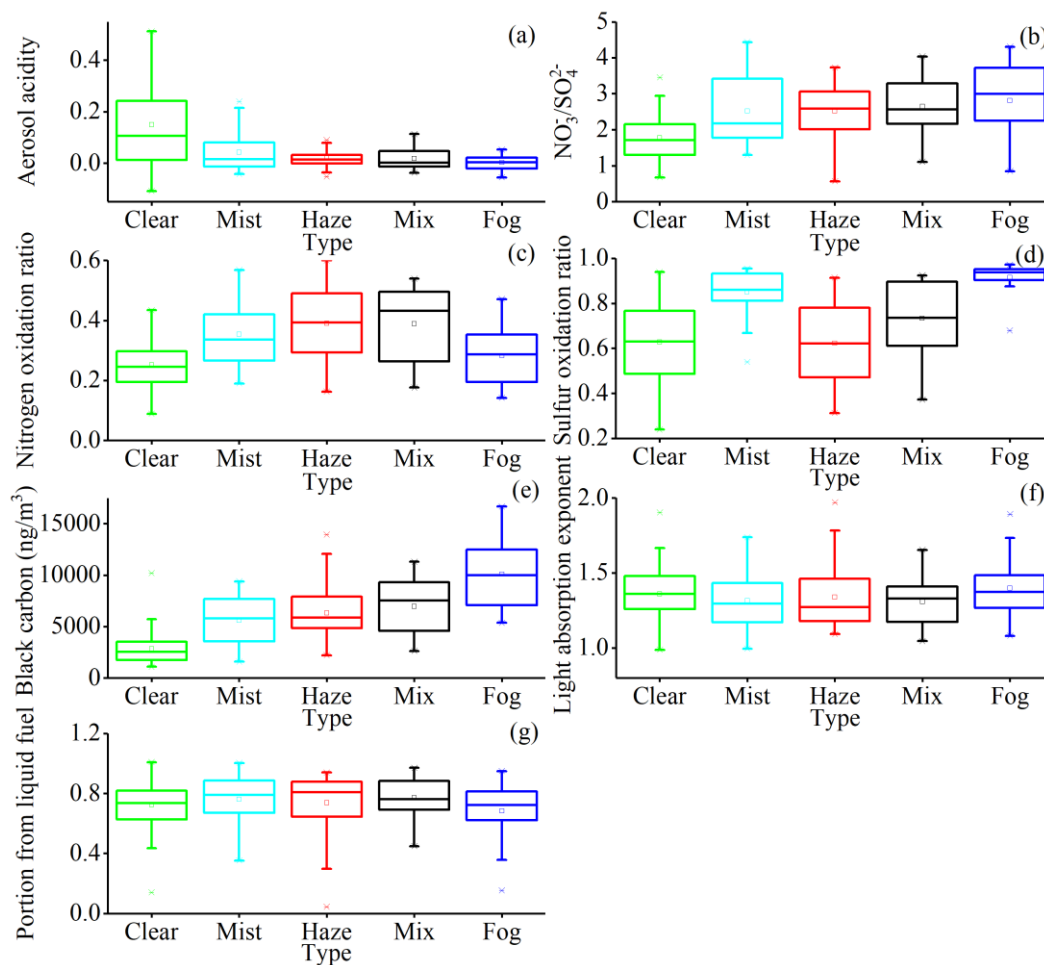


Figure 7. The value of (a) aerosol acidity, (b) $\text{NO}_3^-/\text{SO}_4^{2-}$, (c) nitrogen oxidation ratio, (d) sulfur oxidation ratio, (e) black carbon mass concentration, (f) light absorption exponent, and (g) the portion of the BC contribution from the liquid fuel sources in different process.

3.4.2. Distribution Characteristics of BC in Different Processes

Figure 7e shows that the concentration of BC of $10,119 \text{ ng}\cdot\text{m}^{-3}$ was the highest in the process of fog, which was 3.55 times, 1.80 times, 1.46 times, and 1.60 times that in the processes of clean, mist, haze, and mix, respectively. To ascertain the α values from liquid fuels and solid fuels in Nanjing, the α and p values during the entire observation period were linearly fitted. The results showed that the hourly α in Nanjing was negatively correlated with p , $p = -0.958\alpha + 2.022$, $R^2 = 0.965$. We calculated that $\alpha = 1.1$ ($p = 1$) and $\alpha = 2.1$ ($p = 0$). A previous study [47] in Nanjing also showed similar α values of BC from liquid fuel and solid fuel. Thus, we chose 1.1 for α_{liquid} and 2.1 for α_{solid} in this study. Figure 7f,g show the α and p values in the different process, the average values of α in the clean, mist, haze, mix, and fog processes were 1.36 ± 0.17 , 1.31 ± 0.17 , 1.34 ± 0.19 , 1.31 ± 0.15 , and 1.46 ± 0.30 , respectively, which means that BC from liquid fuel combustion was the main emission during the observation period and the fog process was most affected by solid fuel combustion.

3.5. Effect of $\text{PM}_{2.5}$ Component on Extinction Coefficient in Different Processes

The extinction coefficient β_{ext} obtained by IMPROVE model was linearly fitted with the $\beta_{\text{ext-vis}}$ obtained by the modified Koschmieder relation. Because the visibility of the fog process was too low, the calculated value of $\beta_{\text{ext-vis}}$ was too large and exceeded the calculation range of the IMPROVE model. Thus, the data of the fog process were disregarded in the fitting. As shown in Figure 8, the fitting results show that the extinction contribution of the $\text{PM}_{2.5}$ component during the observation period can

be better calculated by using the IMPROVE model, where $y = 1.519x - 34.929$, $R^2 = 0.818$, and passed the $\alpha = 0.01$ test. The IMPROVE model's calculation results were smaller than the actual extinction coefficient, which was related to the lack of organic matter data and disregard of the organic matter in the calculation.

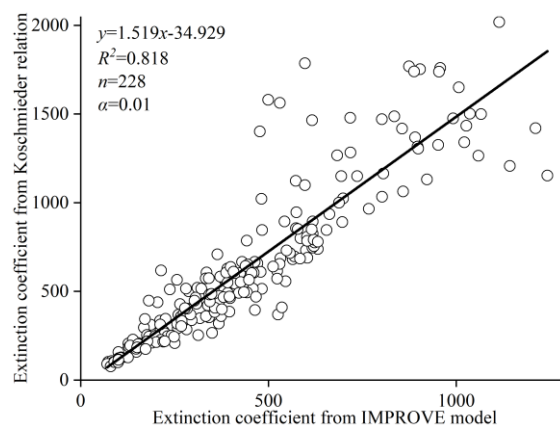


Figure 8. Linear fitting of the extinction coefficient from IMPROVE model and the extinction coefficient from Koschmieder relation.

Figure 9 shows that NO_3^- was always the most important contribution factor of the atmospheric extinction coefficient. The average contribution of NO_3^- to the extinction coefficient of 89.01 Mm^{-1} was lowest in the clean process and highest in the mix process, which was 4.48 times that in the clean process. The proportions of NO_3^- during the clean process and mix process were 46.7% and 60.9%, respectively. The contribution of SO_4^{2-} to the extinction coefficient was different in those processes. The average contribution of SO_4^{2-} to the extinction coefficient was 54.92 Mm^{-1} in the clean process, and the haze process was increased to 2.14 times that in the clean process. The average contribution of SO_4^{2-} to the extinction coefficient was the highest in the fog process and 3.06 times that in the clean process. The average extinction contribution of BC during the clean process was 28.49 Mm^{-1} , which increased to 1.97 times, 2.22 times, 2.44 times, and 3.55 times that of the clean process in the processes of mist, haze, mix, and fog, respectively.

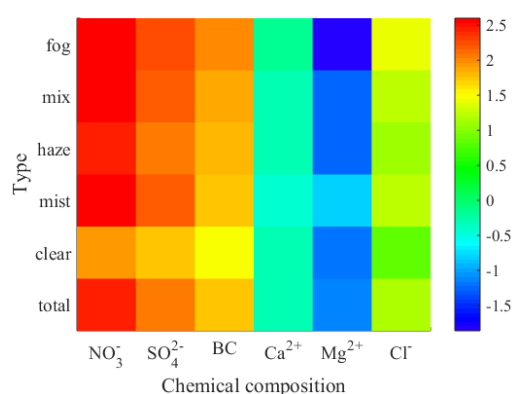


Figure 9. Logarithmic distribution of extinction contribution of each component in different processes in the IMPROVE model.

Among the soil factors, the extinction contribution of Ca^{2+} was approximately six times that of Mg^{2+} . Ca^{2+} has the smallest extinction contribution in the mist process, while Mg^{2+} has the largest extinction contribution in the mist process. The sea salt factor Cl^- has a maximum extinction contribution of 27.26 Mm^{-1} in the fog process, which was approximately 1.6 times that of the mist and mix processes, and the extinction contribution in the clean and haze process was relatively small.

4. Conclusions

The distribution characteristics of pollutants in the processes of clean, mist, haze, mix, and fog during the haze-fog episode in Nanjing were discussed by using high-resolution online observation instruments. The PNSD was variable in different processes and bimodal in the processes of mist and fog, and the particle sizes at peak were 30 nm, 87 nm, 36 nm, and 87 nm. The PNSD was unimodal in the clean process, mix process and haze process, and the particle sizes at peak were 32 nm, 32 nm, and 27 nm, respectively. The PSSD in different processes showed a bimodal distribution, and the second peak of the mix and fog processes shifted to a larger particle size at 480 nm.

The dominant air masses in five processes differed. The air mass in the clean process primarily originated in the northeast direction and the air mass in the haze process primarily originated in the southeast direction, while in the mist, mix, and fog processes they were dominated by local air masses. NO_3^- was the primary component of water soluble ions, which accounted for a minimum of 45.6% in the clean process and a maximum of 53.0% in the mix process. The ratio of NH_4^+ in the different processes was stable at approximately 23%. The ratio of SO_4^{2-} in the clean process and other processes was 26.2% and approximately 20%, respectively.

The aerosol acidity in the clean process was higher than that in other processes. The sources of nitrate and sulfate in different processes primarily comprised secondary transformation, the SOR showed distinct stratification in different RH conditions, and the NOR was relatively high in the haze and mix processes. The sources of nitrogen and sulfur in different processes were mobile sources and the fog process was most affected. The average concentration of BC in the fog processes was $10,119 \text{ ng}\cdot\text{m}^{-3}$, which was 3.55 times, 1.80 times, 1.60 times, and 1.46 times that in the processes of clean, mist, mix, and haze, respectively. In the different processes, BC was primarily based on liquid fuel combustion and the fog process was most affected by solid fuel combustion.

NO_3^- , SO_4^{2-} , and BC were the main contributors to the atmospheric extinction coefficient and contributed more than 90% in different processes. The highest contribution of NO_3^- in the mix process was 398.43 Mm^{-1} . The highest contribution of SO_4^{2-} and BC during the fog process was 167.90 Mm^{-1} and 101.19 Mm^{-1} , respectively.

Author Contributions: Conceptualization, A.L. and H.W.; Methodology, A.L., Y.C., and L.S.; Visualization, A.L., L.S., and S.S.; Investigation, A.L., Y.C., and X.K.; Writing—original draft, A.L. and H.W.; Writing—review and editing, A.L., H.W., Y.Y., Z.W., S.G., K.C., B.Z., and J.W. All authors have read and agreed to the published version of the manuscript.

Funding: This study was supported by the National Natural Science Foundation of China (91644224, 41805096 and 41905026), the special fund of State Key Joint Laboratory of Environment Simulation and Pollution Control (19K03ESPCP), the Natural Science Foundation of Jiangsu Province (BK20180801) and the Natural Science Research Project for Universities of Jiangsu Province, China (18KJB170011).

Conflicts of Interest: The authors declare no conflict of interest.

References

1. Wang, H.; An, J.; Cheng, M.; Shen, L.; Zhu, B.; Li, Y.; Wang, Y.; Duan, Q.; Sullivan, A.; Xia, L. One year online measurements of water-soluble ions at the industrially polluted town of Nanjing, China: Sources, seasonal and diurnal variations. *Chemosphere* **2016**, *148*, 526–536. [[CrossRef](#)] [[PubMed](#)]
2. Wu, J.; Kong, S.F.; Wu, F.; Cheng, Y.; Zheng, S.; Yan, Q.; Zheng, H.; Yang, G.; Zheng, M.; Liu, D.; et al. Estimating the open biomass burning emissions in central and eastern China from 2003 to 2015 based on satellite observation. *Atmos. Chem. Phys.* **2018**, *18*, 11623–11646. [[CrossRef](#)]
3. Ramanathan, V.; Crutzen, P.J.; Kiehl, J.T.; Rosenfeld, D. Aerosols, climate, and the hydrological cycle. *Science* **2001**, *294*, 2119–2124. [[CrossRef](#)] [[PubMed](#)]
4. Andreae, M.O.; Jones, C.D.; Cox, P.M. Strong present-day aerosol cooling implies a hot future. *Nature* **2005**, *435*, 1187–1190. [[CrossRef](#)] [[PubMed](#)]
5. Lohmann, U.; Feichter, J. Global indirect aerosol effects: A review. *Atmos. Chem Phys.* **2005**, *5*, 715–737. [[CrossRef](#)]

6. Chang, D.; Song, Y.; Liu, B. Visibility trends in six megacities in China 1973–2007. *Atmos. Res.* **2009**, *94*, 161–167. [[CrossRef](#)]
7. Ding, Y.; Liu, Y. Analysis of long-term variations of fog and haze in China in recent 50 years and their relations with atmospheric humidity. *Sci. China Earth Sci.* **2014**, *57*, 36–46. [[CrossRef](#)]
8. Zheng, H.; Kong, S.; Yan, Q.; Wu, F.; Cheng, Y.; Zheng, S.; Wu, J.; Yang, G.; Zheng, M.; Tang, L.; et al. The impacts of pollution control measures on PM_{2.5} reduction: Insights of chemical composition, source variation and health risk. *Atmos. Environ.* **2019**, *197*, 103–117. [[CrossRef](#)]
9. Leng, C.; Zhang, Q.; Zhang, D.; Xu, C.; Cheng, T.; Zhang, R.; Tao, J.; Chen, J.; Zha, S.; Zhang, Y.; et al. Variations of cloud condensation nuclei (CCN) and aerosol activity during fog–haze episode: A case study from Shanghai. *Atmos. Chem. Phys.* **2014**, *14*, 12499–12512. [[CrossRef](#)]
10. Fu, W.; Chen, Z.; Zhu, Z.; Liu, Q.; Qi, J.; Dang, E.; Wang, M.; Dong, J. Long-Term Atmospheric Visibility Trends and Characteristics of 31 Provincial Capital Cities in China during 1957–2016. *Atmosphere* **2018**, *9*, 318. [[CrossRef](#)]
11. Deng, Z.; Zhao, C.; Ma, N.; Liu, P.; Ran, L.; Xu, W.; Chen, J.; Liang, Z.; Liang, S.; Huang, M.; et al. Size-resolved and bulk activation properties of aerosols in the north China plain. *Atmos. Chem. Phys.* **2011**, *11*, 3835–3846. [[CrossRef](#)]
12. Zhang, Q.; Meng, J.; Quan, J.; Gao, Y.; Zhao, D.; Chen, P.; He, H. Impact of aerosol composition on cloud condensation nuclei activity. *Atmos. Chem. Phys.* **2012**, *12*, 3783–3790. [[CrossRef](#)]
13. Zhang, S.T. Observation study on characteristics of haze, fog, and haze-fog transition in Nanjing. *Nanjing Uni. Infor. Sci. Technol.* **2015**, *6*, 1–126. (In Chinese)
14. Husar, R.B.; Prospero, J.M.; Stowe, L.L. Characterization of tropospheric aerosols over the oceans with the NOAA advanced very high resolution radiometer optical thickness operational product. *J. Geophys. Res.* **1997**, *102*, 16889–16909. [[CrossRef](#)]
15. Yao, X.; Chan, C.K.; Fang, M.; Cadle, S.; Chan, T.; Mulawa, P.; He, K.; Ye, B. The water-soluble ionic composition of PM_{2.5} in Shanghai and Beijing, China. *Atmos. Environ.* **2002**, *36*, 4223–4234. [[CrossRef](#)]
16. Liu, X.; Zhu, B.; Wang, H.; Zhang, E. Haze variations over 1980–2009 and connecting factors over the Yangtze River Delta Region. *China Environ. Sci.* **2013**, *33*, 1929–1936.
17. Wang, H.; Zhu, B.; Shen, L.; Xu, H.; An, J.; Xue, G.; Cao, J. Water-soluble ions in atmospheric aerosols measured in five sites in the Yangtze River Delta, China: Size-fractionated, seasonal variations and sources. *Atmos. Environ.* **2015**, *123*, 370–379. [[CrossRef](#)]
18. Lu, W.; Wang, H.; Zhu, B.; Shi, S.; Kang, H. Distribution characteristics of PM_{2.5} mass concentration and their impacting factors including meteorology and transmission in North Suburb of Nanjing during 2014 to 2016. *Acta Sci. Cir.* **2019**, *39*, 1039–1048. (In Chinese)
19. Zhang, X.; Wang, Y.; Niu, T.; Zhang, X.; Gong, S.; Zhang, Y.; Sun, J. Atmospheric aerosol compositions in China: Spatial/temporal variability, chemical signature, regional haze distribution and comparisons with global aerosols. *Atmos. Chem. Phys.* **2012**, *12*, 779–799. [[CrossRef](#)]
20. Zhang, X.; Sun, J.; Wang, Y.; Li, W.; Zhang, Q.; Wang, W.; Quan, J.; Cao, G.; Wang, J.; Yang, Y.; et al. Factors contributing to haze and fog in China. *Chin. Sci. Bull.* **2013**, *58*, 1178–1187. (In Chinese)
21. Fu, Q.; Zhuang, G.; Wang, J.; Xu, C.; Huang, K.; Li, J.; Hou, B.; Lu, T.; Streets, D.G. Mechanism of formation of the Heaviest pollution episode ever recorded in the Yangtze river Delta, China. *Atmos. Environ.* **2008**, *42*, 2023–2036. [[CrossRef](#)]
22. Yang, F.; Chen, H.; Du, J.; Yang, X.; Gao, S.; Chen, J.; Geng, F. Evolution of the mixing state of fine aerosols during haze events in Shanghai. *Atmos. Res.* **2012**, *104–105*, 193–201. [[CrossRef](#)]
23. Hu, R.; Wang, H.; Yin, Y.; Chen, K.; Zhu, B.; Zhang, Z.; Kang, H.; Shen, L. Mixing state of ambient aerosols during different fog-haze pollution episodes in the Yangtze River Delta, China. *Atmos. Environ.* **2018**, *178*, 1–10. [[CrossRef](#)]
24. Liu, Z.; Hu, B.; Ji, D.; Cheng, M.; Gao, W.; Shi, S.; Xie, Y.; Yang, S.; Gao, M.; Fu, H.; et al. Characteristics of fine particle explosive growth events in Beijing, China: Seasonal variation, chemical evolution pattern and formation mechanism. *Atmos. Environ.* **2019**, *687*, 1073–1086. [[CrossRef](#)] [[PubMed](#)]
25. Leng, C.; Duan, J.; Xu, C.; Zhang, H.; Wang, Y.; Wang, Y.; Li, X.; Kong, L.; Tao, J.; Zhang, R.; et al. Insights into a historic severe haze event in Shanghai: Synoptic situation, boundary layer and pollutants. *Atmos. Chem. Phys.* **2016**, *16*, 9221–9234. [[CrossRef](#)]

26. Pan, L.; Che, H.; Geng, F.; Xia, X.; Wang, Y.; Zhu, C.; Chen, M.; Gao, W.; Guo, J. Aerosol optical properties based on ground measurements over the Chinese Yangtze Delta Region. *Atmos. Environ.* **2010**, *44*, 2587–2596. [[CrossRef](#)]
27. Kang, H.; Zhu, B.; Su, J.; Wang, H.; Zhang, Q.; Wang, F. Analysis of a long-lasting haze episode in Nanjing, China. *Atmos. Res.* **2013**, *120–121*, 78–87. [[CrossRef](#)]
28. Yu, Y.; Yang, J. Atmospheric extinction of a persistent fog/haze event in Nanjing during December 2007. *Acta Sci. Cir.* **2016**, *36*, 2305–2313. (In Chinese)
29. Wang, L.; Ji, D.; Li, Y.; Gao, M.; Tian, S.; Wen, T.; Liu, Z.; Wang, L.; Xu, P.; Jiang, C.; et al. The impact of relative humidity on the size distribution and chemical process of major water-soluble inorganic ions in the megacity of Chongqing, China. *Atmos. Res.* **2017**, *192*, 19–29. [[CrossRef](#)]
30. Xue, G.; Zhu, B.; Wang, H. Size distributions and source apportionment of soluble ions in aerosol in Nanjing. *Environ. Sci.* **2014**, *35*, 1633–1643. (In Chinese)
31. Qin, Y.; Zhu, B.; Zhou, J.; Pang, B. Characteristics and source apportionment of water-soluble ions in dry deposition in the summer and autumn of Nanjing. *Environ. Sci.* **2016**, *37*, 2025–2033. (In Chinese)
32. Liu, Z.; Gao, W.; Yu, Y.; Hu, B.; Xin, J.; Sun, Y.; Wang, L.; Wang, G.; Bi, X.; Zhang, G.; et al. Characteristics of PM_{2.5} mass concentrations and chemical species in urban and background areas of China: Emerging results from the CARE-China network. *Atmos. Chem. Phys.* **2018**, *18*, 8849–8871. [[CrossRef](#)]
33. Yang, J.; Niu, Z.; Shi, C.; Liu, D.; Li, Z. Microphysics of Atmospheric Aerosols During Winter Haze/Fog Events in Nanjing. *Environ. Sci.* **2010**, *31*, 1425–1431. (In Chinese)
34. Shen, X.; Sun, J.; Zhang, X.; Zhang, Y.; Zhang, L.; Che, H.; Ma, Q.; Yu, X.; Yue, Y.; Zhang, Y. Characterization of submicron aerosols and effect on visibility during a severe haze-fog episode in Yangtze River Delta, China. *Atmos. Environ.* **2015**, *120*, 307–316. [[CrossRef](#)]
35. Jacob, D.J.; Waldman, J.M.; Munger, J.W.; Hoffmann, M. A field investigation of physical and chemical mechanisms affecting pollutant concentrations in fog droplets. *Tellus B Chem. Phys. Meteorol.* **1984**, *36*, 272–285. [[CrossRef](#)]
36. Pandis, S.N.; Seinfeld, J.H.; Pilinis, C. Heterogeneous sulfate production in an urban fog. *Atmos Environ.* **1992**, *26*, 2509–2522. [[CrossRef](#)]
37. Pandis, S.N.; Seinfeld, J.H.; Pilinis, C. The smog-fog-smog cycle and acid deposition. *J. Geophys. Res.* **1990**, *95*, 18489–18500. [[CrossRef](#)]
38. Wang, F.; Zhu, B.; Kang, H.; Gao, J.; Wang, Y.; Jiang, Q. Analysis of the impact of two typical air pollution events on the air quality of Nanjing. *Environ. Sci.* **2012**, *33*, 3647–3655. (In Chinese)
39. Makkonen, U.; Virkkula, A.; Mäntykenttä, J.; Hakola, H.; Keronen, P.; Vakkari, V.; Aalto, P.P. Semi-continuous gas and inorganic aerosol measurements at a Finnish urban site: Comparisons with filters, nitrogen in aerosol and gas phases, and aerosol acidity. *Atmos. Chem. Phys.* **2012**, *12*, 5617–5631. [[CrossRef](#)]
40. Wang, H.; An, J.; Shen, L.; Zhu, B.; Pan, C.; Liu, Z.; Liu, X.; Duan, Q.; Liu, X.; Wang, Y. Mechanism for the formation and microphysical characteristics of submicron aerosol during heavy haze pollution episode in the Yangtze River Delta, China. *Sci. Total Environ.* **2014**, *490*, 501–508. [[CrossRef](#)]
41. Zou, J.; An, J.; Wang, H.; Shao, P.; Duan, Q.; Xue, G.; Pang, B. Distribution Characteristics of Pollution Gases and Water Soluble Ion in Aerosol During the Asian Youth Games of Nanjing. *Environ. Sci.* **2014**, *35*, 4044–4051. (In Chinese)
42. Liao, B.; Wu, D.; Chang, Y.; Lin, Y.; Wang, S.; Li, F. Characteristics of particulate SO₄²⁻, NO₃⁻, NH₄⁺ and related gaseous pollutants in Guangzhou. *Acta Sci. Cir.* **2014**, *34*, 1551–1559. (In Chinese)
43. Liu, A.; Wang, H.; Chen, K.; Lu, W.; Shi, S.; Liu, Z. Distribution characteristics of water-soluble ions during a haze pollution process in Nanjing. *China Environ. Sci.* **2019**, *39*, 1793–1803. (In Chinese)
44. Huang, J.; Chen, Z.; Mo, Z.; Li, H.; Liu, H.; Li, H.; Liang, G.; Yang, J.; Zhang, D.; Li, Y. Analysis of characteristics of water-soluble ions in PM_{2.5} in Guilin based on the MARGA. *China Environ. Sci.* **2019**, *39*, 1390–1404. (In Chinese)
45. Li, Y.; Zhou, H.; Zhang, Z.; Wang, Q.; Luo, L. Pollution characteristics of secondary water-soluble inorganic ions of PM_{2.5} in urban Chengdu. *Environ. Sci.* **2014**, *35*, 4439–4445. (In Chinese)
46. Liu, Y.; Yan, C.; Zheng, M. Source apportionment of black carbon during winter in Beijing. *Sci. Total Environ.* **2018**, *618*, 531–541. [[CrossRef](#)]
47. Jing, A.; Zhu, B.; Wang, H.; Yu, X.; An, J.; Kang, H. Source apportionment of black carbon in different seasons in the northern suburb of Nanjing, China. *Atmos. Environ.* **2019**, *201*, 190–200. [[CrossRef](#)]

48. Sisler, J.F.; Malm, W.C. Interpretation of trends of PM_{2.5} and reconstructed visibility from the IMPROVE network. *J. Air Waste Manage. Assoc.* **2000**, *50*, 775–789. [[CrossRef](#)]
49. Malm, W.C.; Day, D.E. Estimates of aerosol species scattering characteristics as a function of relative humidity. *Atmos. Environ.* **2001**, *35*, 2845–2860. [[CrossRef](#)]
50. Jiang, L.; Zhang, Z.; Zhu, B.; Shen, Y.; Wang, H.; Shi, S.; Sha, D. Comparison of parameterizations for the atmospheric extinction coefficient in Lin'an, China. *Sci. Total Environ.* **2018**, *621*, 507–515. [[CrossRef](#)]
51. Zhang, Z.; Shen, Y.; Li, Y.; Zhu, B.; Yu, X. Analysis of extinction properties as a function of relative humidity using a κ -EC-Mie model in Nanjing. *Atmos. Chem. Phys.* **2017**, *17*, 4147–4157. [[CrossRef](#)]
52. McCartney, E.J.; Pan, N.X. *Optics of the Atmosphere: Scattering by Molecules and Particle*; Science Press: Beijing, China, 1988; pp. 1–413. (In Chinese)
53. Schichtel, B.A.; Husar, R.B.; Falke, S.R.; Wilson, W.E. Haze trends over the United States, 1980–1995. *Atmos. Environ.* **2001**, *35*, 5205–5210. [[CrossRef](#)]
54. Lillis, D.; Cruz, C.N.; Collett, J., Jr.; Richards, L.W.; Pandis, S.N. Production and removal of aerosol in a polluted fog layer: Model evaluation and fog effect on PM. *Atmos. Environ.* **1999**, *33*, 4797–4816.
55. Zhang, L.; Sun, J.; Shen, X.; Zhang, Y.; Che, H.; Ma, Q.; Zhang, Y.; Ogren, J.A. Observations of relative humidity effects on aerosol light scattering in the Yangtze River Delta of China. *Atmos. Chem. Phys.* **2015**, *15*, 8439–8454. [[CrossRef](#)]
56. Kulmala, M.; Laaksonen, A.; Charlson, R.J.; Korhonen, P. Clouds without supersaturation. *Nature* **1997**, *388*, 336–337. [[CrossRef](#)]
57. Yin, Y.; Dong, Y.; Wei, Y.; Wang, T.; Li, J.; Yang, W.; Fan, S. The analysis of chemistry composition of fine mode particles in Nanjing. *Tran. Atmos. Sci.* **2009**, *32*, 723–733. (In Chinese)



© 2020 by the authors. Licensee MDPI, Basel, Switzerland. This article is an open access article distributed under the terms and conditions of the Creative Commons Attribution (CC BY) license (<http://creativecommons.org/licenses/by/4.0/>).